Interband scattering across the Lifshitz transition in WTe_2

Sruthi S,[1] Deepa S. Narang,[1] Prasad Vishnubhotla,[1] Arnab Bera,[2] Sk Kalimuddin,[2] Kenji Watanabe,[3] Takashi Taniguchi,[4] Mintu Mondal,[2] and Aveek Bid[1,*]

[1]*Department of Physics, Indian Institute of Science, Bangalore, India 560012*

[2]*Department of Physics, Indian Association for the Cultivation of Science, Kolkata, India 700032*

[3]*Research Center for Functional Materials, National Institute for Materials Science, 1-1 Namiki, Tsukuba 305-0044, Japan*

[4]*International Center for Materials Nanoarchitectonics, National Institute for Materials Science, 1-1 Namiki, Tsukuba 305-0044, Japan*

(Received 14 June 2022; revised 15 August 2022; accepted 8 September 2022; published 16 September 2022)

In this paper, we investigate the resistance fluctuations near the Lifshitz transition in WTe_2 devices. We identify the Lifshitz transition from electrical and thermal transport studies. The band structure obtained at low temperatures using quantum oscillation measurements consists of two hole pockets and two electron pockets at the Fermi energy, the hole pockets vanish above the Lifshitz transition temperature. The electrical noise shows a conspicuous peak near the Lifshitz transition temperature; we establish this noise to be arising from charge carrier scattering between the Weyl nodes and proximate areas of the bands. Our comparative study of the noise on WTe_2 devices fabricated on substrates with different scattering mechanisms elucidates the effect of interband scattering on the physics of Weyl semimetals.

DOI: 10.1103/PhysRevB.106.115421

I. INTRODUCTION

A system undergoes a Lifshitz transition when its band topology changes under external perturbations like temperature, strain, doping, electric field, or pressure [1]. This transition, which does not involve any symmetry breaking, is characterized by the appearance of zeros in the energy spectrum of a many-body fermionic system. The modification of the low-energy excitation spectra often leads to interesting changes in the electronic, magnetic, and optical properties [2,3]. Examples of such topological transitions are spiral order in magnets, charge density waves in metals, superconductivity, and superfluidity [4–11].

Among the low-dimensional systems that undergo a Lifshitz transition, transition metal ditellurides like WTe_2 and $MoTe_2$ have attracted special attention. In the specific case of T_d-WTe_2, an extremely large magnetoresistance [12,13], superconductivity (induced through pressure [14–16], proximity effects [17,18], gating [19], and intercalation [20]), ferroelectricity at room temperature [21], enhanced Nernst signal [22], and quantum spin Hall effect in its single-layer form [23–25] make it a model system to test various theories [26,27]. Important for our purposes,WTe_2 is a type-II Weyl semimetal with tilted Weyl cones. Consequently, when the the Fermi energy (E_F) is at the Weyl node, the electron and the hole bands touch each other [28–31]. It is thus instructive to investigate the effect of charge-carrier scattering at the Weyl nodes on the topological transport properties like Chiral anomaly [32–35]. Unfortunately, barring one notable recent exception [36], this topic has not been adequately addressed by the community.

T_d-WTe_2 undergoes a Lifshitz transition between a phase with four bands (two electron and hole pockets each) and a phase with two bands (two hole pockets) along the $X-\Gamma-X$ direction on the Fermi surface at a critical temperature T_L. The transition is driven by the strong temperature dependence of the chemical potential caused by the proximity of the electron and hole bands [37]. T_L is thickness dependent and is best detected through spectroscopic techniques like angle-resolved photoemission spectrorscopy (ARPES) [38]. In transport studies, the Lifshitz transition is generally identified via scaling of the magnetoresistance using Kohler's rule and by a sudden change in the ratio of the number density of the itinerant electrons and holes [39,40]. For systems having a high Lifshitz transition temperature, quantum oscillations cannot be used to deduce the band structure change due to thermal smearing effects. In three-dimensional (3D) systems, a Lifshitz transition can also be detected from thermal measurements [41]; this however becomes unfeasible in lower-dimensional systems where it is incredibly challenging to determine the minute changes in thermoelectric coefficients that signal this transition.

In this paper, we establish, through resistance fluctuation spectroscopy studies, that the Lifshitz transition has a profound influence on the charge carrier dynamics in T_d-WTe_2. Specifically, we demonstrate that the scattering of the charge carriers at the Weyl nodes near the Lifshitz transition is predominantly by long-range isotropic defect potentials. Our work provides insight into the charge-carrier dynamics at the topological nodes in Weyl and Dirac fermionic systems. It establishes a benchmark for the quality of samples required to see the physics of Weyl nodes unambiguously.

II. RESULTS

A. Transport measurements

T_d-WTe_2 flakes were obtained on a silicone elastomer polydimethylsiloxane (PDMS) from a bulk crystal by the

*Author to whom correspondence should be addressed: aveek@iisc.ac.in

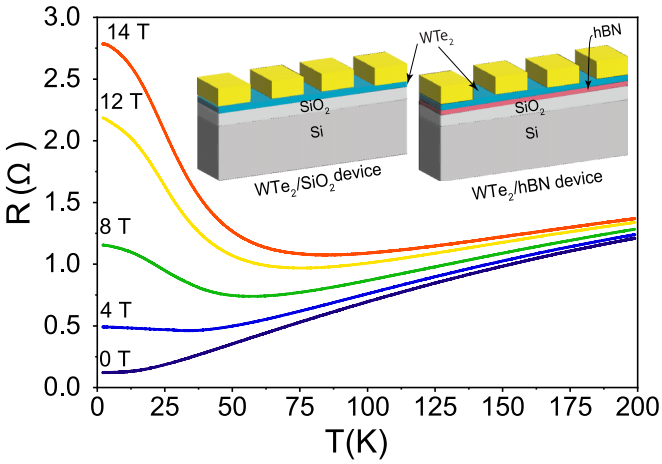

FIG. 1. Plot of the resistance versus temperature of WTe_2 at different magnetic fields. Insets: Schematics of the two types of devices.

well-established mechanical exfoliation technique [42–44]. The crystals, grown by the flux growth technique, were procured commercially from 2D semiconductors [45]. Isolated flakes of T_d-WTe_2 of thickness ∼125 nm [identified through atomic force microscopy were transferred from the PDMS onto Cr/Au electrical contacts (prepared using standard electron-beam lithography) on the substrate (for details see Ref. [46]). We used two substrates that offer very distinct charge carrier scattering mechanisms. The first, 285 nm SiO_2 on top of Si^{++}, is known to host dangling bonds that affect the charge carriers in the transport channel of the material on top (in this case, T_d-WTe_2) via strong, short-ranged interactions. The second is single-crystalline hBN flakes on top of SiO_2/Si^{++} – here, short-range scattering is almost entirely eliminated, and the charge carriers are affected by long-range Coulomb interactions [47]. We refer to these as WTe_2/SiO_2 devices and WTe_2/hBN devices, respectively (see inset of Fig 1). The entire sample fabrication process, in both cases, was performed inside an N_2 filled glove box with O_2 concentration <0.1 ppm to avoid degradation of the WTe_2.

Figure 1 shows the temperature dependence of the resistance of the WTe_2/SiO_2 device over a temperature range 2 K < T < 200 K at different perpendicular magnetic fields, B. At 0 T, the resistivity has a metallic behavior down to 2 K. For $B > 4$ T, dR_{xx}/dT is positive down to a certain temperature T_t, below this temperature, dR_{xx}/dT becomes negative. The value of T_t increases from 33 K at 4 T to 85 K at 14 T. This so-called turn-on behavior is considered an indication of a high-quality and low charge carrier density sample [48].

B. Thermoelectric measurements

To verify the presence of Lifshitz transition, we measured the Seebeck coefficient S of the bulk crystal as shown in Fig. 2 [22,49]. The measurement was done on the bulk crystal of T_d-WTe_2. The flakes used for transport measurement are cleaved from the same bulk crystal. The negative value of S suggests that electron-type carriers dominate the thermoelectric transport in measurement temperature range of interest. For standard conductors where electron-electron interaction is negligible, the Seebeck coefficient is often described using the following the semiclassical Mott formula [50]:

$$S = -\frac{\pi^2}{3}\frac{k_B^2 T}{e}\left\{\frac{\partial\, ln(\tau v S_F)}{\partial \epsilon}\right\}_{\epsilon=\epsilon_F}. \quad (1)$$

Here, v is the Fermi velocity, S_F is the Fermi surface area and τ is the scattering/relaxation time. Generally, the scattering time, the Fermi velocity and the Fermi surface area are energy independent leading to a simple linear-in-temperature form as per the above equation. However, the modifications in Fermi surface area, S_F can lead to the significant change in the Seebeck coefficient [51].

Figure 2(a) shows a sharp kink in the T dependence of S and the corresponding discontinuity in the T dependence of $dSdT$ [Fig. 2(b)] can be associated with the reconstruction of Fermi surface due to the Lifshitz transition in bulk T_d-WTe_2 at $T_L^{TE} = 147$ K. We attribute the slight difference between T_L and T_L^{TE} to the thickness difference of the sample studied, while we measured the Seebeck coefficient on a bulk crystal, transport measurements used to extract T_L were performed on T_d-WTe_2 flakes exfoliated from the bulk crystal.

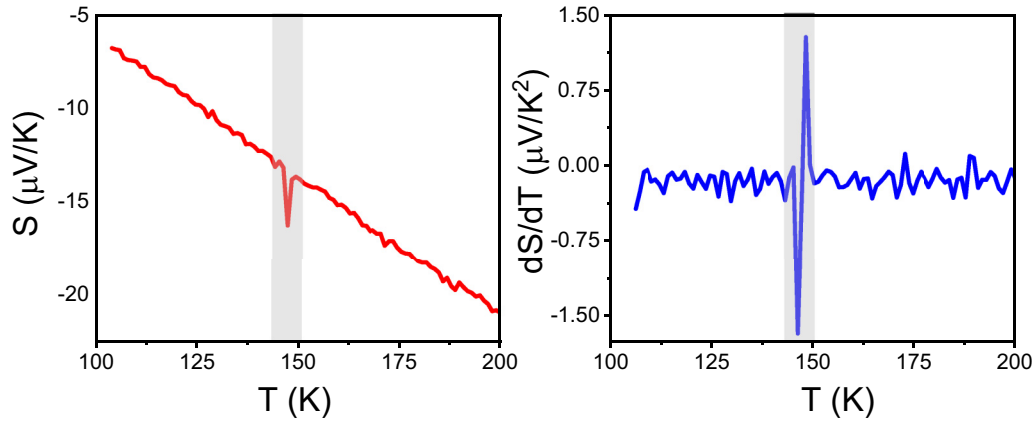

FIG. 2. (a) The Seebeck coefficient S and (b) dS/dT versus temperature in the heating cycle. The shaded regions in both (a) and (b) show the Lifshitz transition temperature.

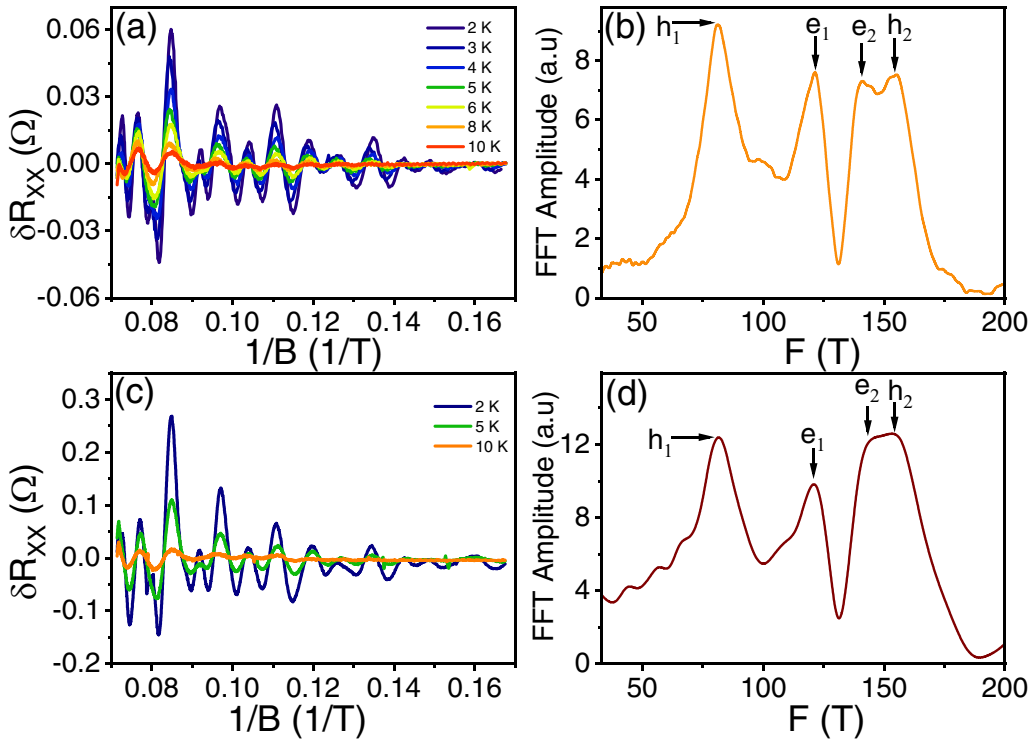

FIG. 3. (a) Plot of the longitudinal magnetoresistance versus $1/B$ after background subtraction at different temperatures for WTe_2/SiO_2. (b) Frequency spectrum of the SdH oscillations obtained at $T = 2$ K. h_1 and h_2 are the frequencies corresponding to the two hole pockets while e_1 and e_2 correspond to the two electron pockets WTe_2/SiO_2. (c) Plot of the longitudinal magnetoresistance versus $1/B$ after background subtraction at different temperatures for WTe_2/hBN. (d) Frequency spectrum of the SdH oscillations obtained at $T = 2$ K for WTe_2/hBN.

C. Band structure from quantum oscillations

Figure 3(a) is the plot of the Shubnikov–de Haas (SdH) oscillations in the WTe_2/SiO_2 device as a function of $1/B$. The Fast Fourier transform of the SdH oscillations gives four distinct frequencies at $h_1 = 81$ T, e_1=121 T, e_2=141 T and h_2=155 T [see Fig. 3(b)]. h_1 and h_2 corresponds to the two hole pockets, while e_1 and e_2 correspond to two electron pockets [52,53]. With increasing temperature, the amplitude of the oscillations diminishes [54]. We extract the effective mass m^* by fitting the temperature dependence of the normalized δR_{xx} to the Lifshitz-Kosevich equation [55]:

$$\delta R_{xx} \propto \frac{2\pi k_B m^* T}{\hbar e B} sinh\left(\frac{2\pi k_B m^* T}{\hbar e B}\right). \quad (2)$$

The average value of m^* extracted from the fits is 0.44 m_e, where m_e is the mass of the free electron. The transport scattering time τ_{tr}=0.94 ps was calculated from the values of μ and m^*. From the Dingle plots of the quantum oscillation data, we find the value of the quantum lifetime to be τ_Q =0.3 ps.

D. Resistance fluctuation spectroscopy

Having established the Lifshitz transition and the low-temperature band-structure in T_d-WTe_2, we turn our attention to dynamics of charge carriers at the Fermi surface near $T = T_L$ through resistance fluctuation spectroscopy studies. The low-frequency resistance fluctuation measurements were performed over a temperature range of 85 to 200 K using a four-probe digital signal processing technique. Briefly, a dual-channel lock-in amplifier was used to bias the device with an AC current of rms value 40 μA at a carrier frequency of 228 Hz. The voltage drop across the device was amplified using a low-noise preamplifier (SR554) and subsequently detected by the lock-in amplifier (for details of the measurement technique, see our previous publications [46,56,57]). The temperature of the cryostat insert was controlled to better than 5 mK using a temperature controller. The resistance fluctuations at each temperature were recorded for 30 min at a sampling rate of 2048 data points/s using a 16-bit analog-to-digital converter. The time series of the resistance fluctuations were digitally decimated and antialiased filtered. The power spectral density (PSD) of the resistance fluctuations, $S_R(f)$, was calculated over a spectral frequency range of 7 mHz$<f<$7 Hz from the filtered time series using the Welch periodogram method.

The time series of the resistance fluctuations measured at a few representative temperatures for the WTe_2/SiO_2 device are plotted in Fig. 4(a) [Fig. 5(a) for WTe_2/hBN device]; the data have been vertically shifted for clarity. Figure 4(b) shows the PSD of these time series; the data have been multiplied by f to detect any deviations from $1/f$ nature. At 100 and at 200 K, the PSD has an inverse dependence on f. But over a narrow intervening range of temperatures 152 K $< T <$ 160 K, the PSD deviates from the $1/f$ dependence on the spectral frequency. The corresponding data for the WTe_2/hBN device are presented in Fig. 5(b).

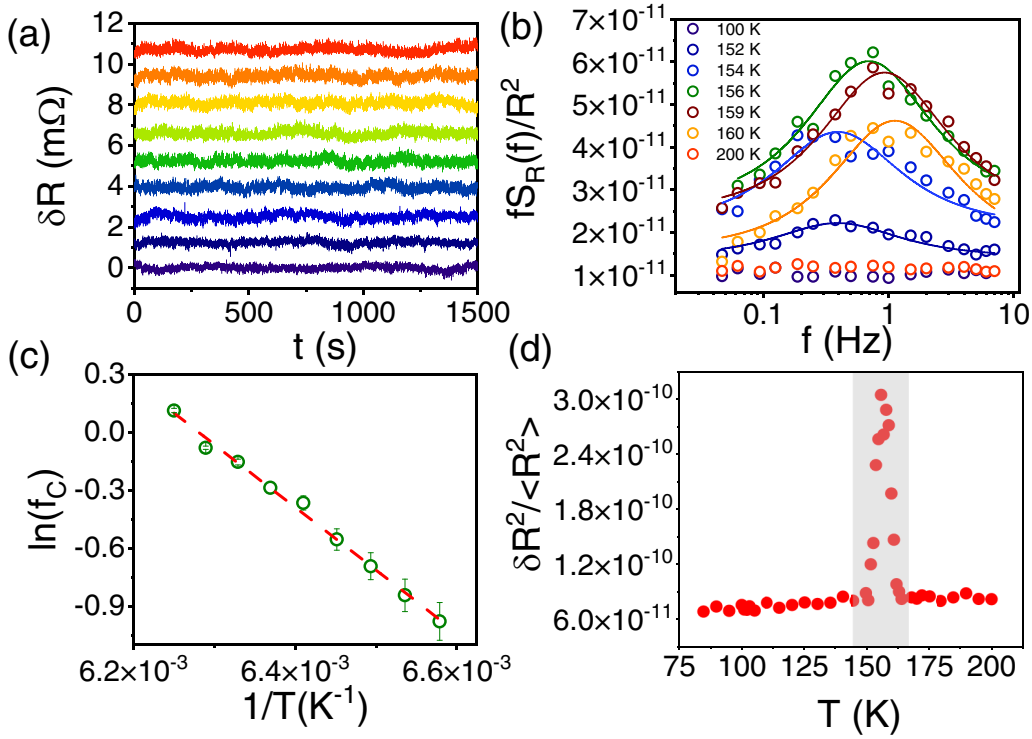

FIG. 4. (a) Plot of the time-series of resistance fluctuations for the WTe_2/SiO_2 device at a few representative temperatures ranging from 152 to 160 K in steps of 1 K. (b) Plots of the scaled PSD $fS_R(f)/R^2$ versus f at different temperatures. The measured data are shown as scatter plot, the solid lines are fits using Eq. (3). (c) Plot of f_c as a function of $1/T$; the green open circles are the data extracted from Eq. (3) and the dotted red line is the fit to the Arrhenius relation. (d) Plot of the relative variance of resistance fluctuations versus T – the shaded region highlights the sharp peak near $T = T_L$.

We fit the scaled PSD of the resistance fluctuations to the following equation (see Figs. 3):

$$f\frac{S_R(f)}{R^2} = A + \frac{Bff_c}{\left(f^2 + f_c^2\right)}. \tag{3}$$

The first term on the right-hand side quantifies the contribution to the total noise from the $1/f$ component; the second term is the Lorentzian component. These fits to the data (solid lines in the two figures) confirms the presence of a Lorentzian component in the spectrum of the resistance fluctuations along with the ubiquitous $1/f$ noise.

The relative variance of the resistance fluctuations was calculated by integrating $S_R(f)$ over the measured frequency bandwidth:

$$\mathcal{R} = \frac{\langle \delta \mathrm{R}^2 \rangle}{\langle \mathrm{R}^2 \rangle} = \frac{1}{\mathrm{R}^2}\int_{0.007\ \mathrm{Hz}}^{7\ \mathrm{Hz}} \mathrm{S_R(f)df}. \tag{4}$$

The T dependence of $\mathcal{R}$ are shown in Figs. 4(d) and 5(d). We observe a sharp peak over a narrow temperature window $151\ K < T < 162\ K$; this window coincides with the T range over which the Lorentzian noise is seen. One notable difference in the case of the WTe_2/hBN device is the appearance of a secondary peak in $\mathcal{R}$ at $T = 200$ K [Fig. 5(d)]. This second peak is very close to the temperature where an additional Lifshitz transition has been seen in T_d-WTe_2 through ARPES measurements [38]. The origin of this additional Lifshitz transition is debated in the community with most authors attributing it to the second hole band moving below E_F.

III. DISCUSSION

To summarize our observations, T_d-WTe_2 has two noise sources near the Lifshitz transition – (1) a $1/f$ part and (2) a Lorentzian part. Additionally, the integrated noise has a sharp peak around T_L. Below we propose a possible origin of these two very distinct noise phenomena.

Fluctuations with a Lorentzian line shape arises when the value of the fluctuating quantity toggles between two well-defined values (random telegraphic noise). Physically, this usually happens when there are two energetically equivalent states accessible to the system with the time scale of switching between the two states $\tau = 1/f_c$ [58]. We find the values of f_c are thermally activated: $f_c = f_0 e^{-E_a/K_B T}$ [59] with an activation energy $E_a = 280 \pm 8$ meV for the WTe_2/SiO_2 device [Fig. 4(c)].The value of activation energy associated with the secondary peak (seen only in the WTe_2/hBN device) is $E_a = 447 \pm 15$ meV [Fig. 5(c)]. We speculate that this energy scale most likely corresponds to the to the trapping-detrapping energies of the charge carriers at the interface between WTe_2 and the substrate. Note that the random telegraphic noise is not apparent in the time series of resistance fluctuations as it is masked by larger amplitude $1/f$ fluctuations.

Resistance fluctuations with a $1/f$ spectrum in a conductor can have two independent origins: fluctuations in the mobility or fluctuations in the charge carrier number density – $\mathcal{R} = \delta\langle R^2\rangle/\langle R^2\rangle = \delta\langle n^2\rangle/\langle n^2\rangle + \delta\langle \mu^2\rangle/\langle \mu^2\rangle$ [60,61]. In materials with moderately high-mobility and low number density materials, like T_d-WTe_2, number density fluctuations dominates.

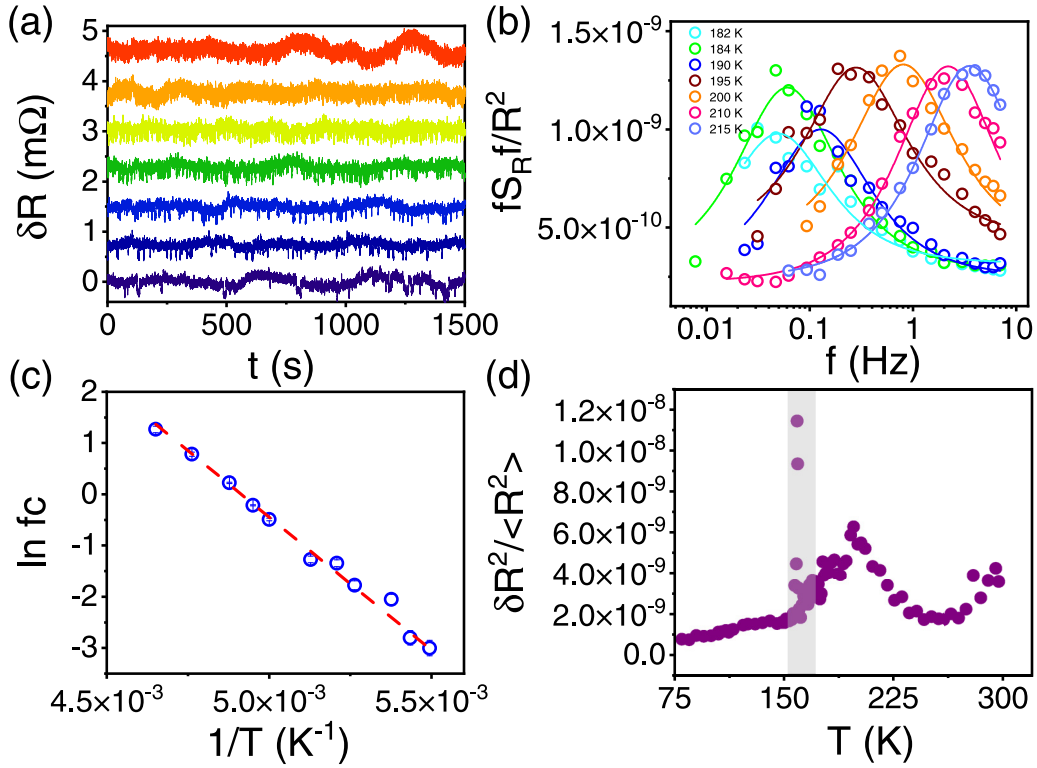

FIG. 5. (a) Plot of the time-series of resistance fluctuations for the WTe_2/hBN device at a few representative temperatures ranging from 182 to 215 K. (b) Plots of the scaled PSD $fS_R(f)/R^2$ versus f at different temperatures. The measured data are shown as scatter plot, the solid lines are fits using Eq. (3). (c) Plot of f_c as a function of $1/T$; the blue open circles are the data extracted from Eq. (3) and the dotted red line is the fit to the Arrhenius relation. (d) Plot of the relative variance of resistance fluctuations versus T; the shaded region highlights the sharp peak near $T = T_L$. There is an additional peak in the noise for the WTe_2/hBN device at T = 200 K. This peak T = 200 K arises from an additional Lifshitz transition seen in WTe_2 through ARPES measurements [38]

The contribution of mobility fluctuations to the measured noise in such materials is much smaller by comparison [62]. In the specific case of T_d-WTe_2, these fluctuations arise due to the strong scattering at the Weyl node [35,63]. From transport measurements, we find that the ratio of the transport scattering time τ_{tr} and the quantum scattering time τ_Q to be $\tau_{tr}/\tau_Q = 3$ at 2 K for the WTe_2/SiO_2 device. Recall that in systems with $\tau_{tr}/\tau_Q > 1$, the scattering of the charge carriers is anisotropic and is primarily due to long-range disorder arising from screened Coulomb potentials [64]. For charge carriers to scatter from a Weyl node to some other band, the relevant quantity is $\delta k\xi$, where δk is the change in the wave-vector, and ξ is the defect correlation length. $\delta k\xi$ values were taken from the theoretical calculation done in Ref. [36]. We estimate that for the WTe_2/SiO_2 device, $\delta k\xi \approx 1$. This value indicates a strong coupling between the Weyl point and some other point in the reciprocal space opening up a large phase space for carrier scattering. The effect of this is most striking near $T = T_L$ where the Weyl nodes come close to E_F with the interband scattering leading to random telegraphic noise and consequently, a large increase in resistance fluctuations at $T = T_L$.

In the case of the WTe_2/hBN device, $\tau_{tr}/\tau_Q \sim 30$ at 2 K, implying that the scattering is extremely anisotropic (with strong suppression of backscattering) and is primarily due to remote ionized impurities [65]. A direct consequence of the anisotropic scattering is that the effect of interband scattering has a stronger effect on the resistance fluctuations than that from intraband scattering processes. To get a quantitative understanding of the magnitude of the measured resistance fluctuations, one needs a comprehensive understanding of the inter-band scattering processes in a Weyl semimetal. To the best of our knowledge, a theory that completely encompasses this process is missing. Comparing the excess noise at T_L in the two types of devices two distinctions become obvious: (1) the noise peak at T_L in WTe_2 /SiO_2 is much sharper as compared to the WTe_2/hBN device and (2) there is an additional peak in the noise for the WTe_2/hBN device at T = 200 K. The large increase in τ_{tr}/τ_Q with increasing device quality translates to an increase in $\delta k\xi$, which in turn is predicted to lead to an exponential increase in the visibility of topological features like chiral anomaly [36]. The larger mobility measured for devices fabricated on hBN (as compared to those on SiO_2) is usually attributed only to the suppression of impurity scattering at the interface. Our study establishes that the nature of disorder scattering from the substrate (short-range for SiO_2 and long-range for hBN) is also an important parameter that significantly affects the device mobility [66]. Our observations establish that in the high-quality devices, resistance fluctuation spectroscopy can identify topological phase transitions that standard transport measurements cannot resolve; a case in

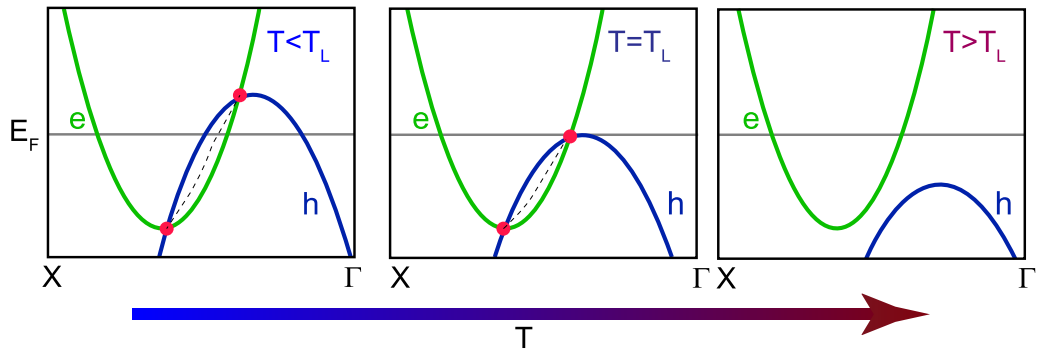

FIG. 6. Schematic showing the temperature evolution of the electron and the hole bands with T for T_d-WTe_2 as it undergoes the Lifshitz transition. The electron and hole bands are shown by green and blue lines respectively, the red filled circles are the Weyl nodes and the dashed black lines are the Fermi arcs. For simplicity, we show only one each of the electron and the hole bands.

point being the second Lifshitz transition in the WTe_2/hBN device.

For $T < T_L$, both the hole and the electron bands are occupied (see Fig. 6 for a schematic). At temperatures far away from T_L, the number of both electrons and holes is significant, and consequently, the relative variance of resistance fluctuations is insignificant. With increasing T, the hole band moves down in energy, and at $T = T_L$, it touches the Fermi energy. As $T \to T_L$, the number density of the hole bands decreases drastically. The combined effect of the decrease in the number of holes and the enhanced scattering at the Weyl points lead to a sharp increase in $\delta\langle n^2\rangle/\langle n^2\rangle$ and to the observed peak in $\mathcal{R}$ for 151 K $< T <$ 162 K. Beyond T_L, electrons are the only charge carriers in the system, the Weyl nodes vanish, and the measured resistance fluctuations again go down.

Over the last few years, there has been a growing consensus in the community that electrical transport in such multiband systems is substantially modulated by strong conductance fluctuations arising from interband scattering processes. In the case of type-II Weyl semi-metals, where the electron and hole bands cross at the Weyl points, such conductance fluctuations lead to a negative longitudinal magnetoresistance [67] which, in some cases, is strong enough to wholly mask the effects of topological phenomenon like Chiral anomaly [68]. In this paper we propose that the resistance fluctuations across the Lifshitz transition in the type-II semimetal WTe_2 is dominated by interband scattering at the Weyl points. Our study establishes the need for high-quality samples to detect the exciting science of Weyl semimetals.

ACKNOWLEDGMENTS

A.B. acknowledges funding from DST FIST program and DST (No. DST/SJF/PSA01/2016-17). D.S.N. thanks DST for Woman Scientist fellowship (WOS-A) (Grant No. SR/WOS-A//PM-98/2018).

S.S. and D.S.N. contributed equally to this work.

APPENDIX A: THERMOELECTRIC MEASUREMENTS IN BOTH HEATING AND COOLING CYCLE

The thermoelectric power measurement of bulk T_d-WTe_2 single crystal was done in both the heating and cooling cycle. Measured thermoelectric data is presented in Fig. 7, which unambiguously confirms a sharp transition near 147 K due to the Lifshitz transition of T_d-WTe_2. Since the Fermi surface reconstruction due to the Lifshitz transition is very sharp near the transition, we see sharp kink in both heating and cooling cycle (S vs T data) near the transition without any noticeable hysteresis.

APPENDIX B: ELIMINATION OF BACKGROUND NOISE

The measurements were performed using a dual channel method wherein the bias-independent noise component (typically the sum of thermal noise from the sample, $1/f$ noise from the amplifier, and other spurious noise sources) appears as a quadrature component of the output voltage of the lock-in amplifier. We call this the background signal. On the other hand, the in-phase component of the output voltage of the lock-in-amplifier is a sum of the bias-dependent noise from the device and background noise. The power spectral density of $\delta V(t)$ at the output of the lock-in-amplifier is given by [69,70]:

$$S_V(f,\delta) \simeq G_0^2\left[S_V^0(f_0 - f) + I_0^2 S_R(f)cos^2(\delta)\right], \qquad \text{(B1)}$$

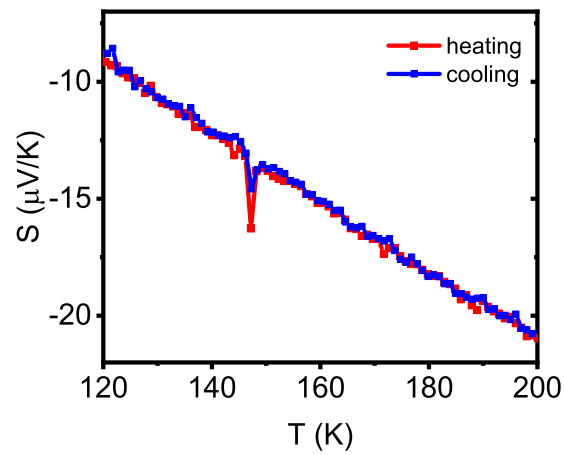

FIG. 7. The Seebeck coefficient (S) versus temperature (T) in the heating and cooling cycle.

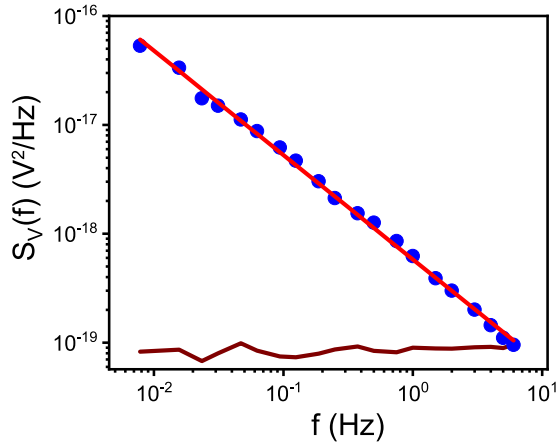

FIG. 8. Spectrum showing $1/f$ noise (blue circles) and background noise (Wine color solid line). Red color solid line shows the $1/f$ fit. The noise measurement is done in T_d-WTe_2 at 5K using SR 554 transformer preamplifier.

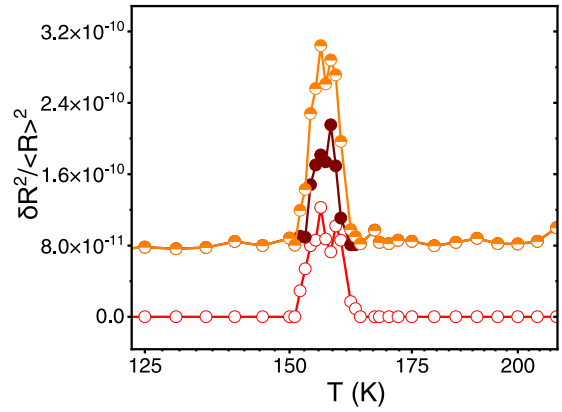

FIG. 9. Plot showing the contribution of $1/f$ (solid brown circles) and Lorentzian components (Open red circles) to the resistance fluctuations. Total noise is shown in half-filled orange circles.

where G_0 is the product of the gain of the preamplifier and the LIA, S_V^0 is the power spectral density due to the background fluctuation and is not related to the sample noise, f is the measurement frequency, f_0 is the excitation frequency, I_0 is the RMS value of the biasing current, δ is the relative phase between the source current and the input of the phase-sensitive detector of the lock-in amplifier, $S_R(f)$ is the PSD of resistance fluctuation of the sample ($S_V(f) = I_0^2 S_R(f)$). The additional noise contribution arising from different electrical components of the measurement setup is low or eliminated properly so that the main contribution to the Johnson-Nyquist noise is $S_V^0 \approx 4k_BTR$ [71].

When $\delta = 0$ (in-phase component of the signal):

$$S_V(f,0)/G_0^2 \simeq S_V^0 + S_V(f), \tag{B2}$$

while for $\delta = \pi/2$ (quadrature component of the signal);

$$S_V(f,\pi/2)/G_0^2 \simeq S_V^0. \tag{B3}$$

The time series of these two (in-phase and quadrature) components are measured simultaneously. Subtracting the power spectral density of the background noise from that of the in-phase component gives us the bias-dependent noise from the device, uncontaminated by amplifier noise or other background noises [72–74]. Details of the technique can be found here [57]. Before each measurement, we calibrate the system by measuring the noise of a standard resistor. We ensure that the measured voltage fluctuations $\delta\langle V^2\rangle$ (from which we extract the resistance fluctuations using $\delta\langle R^2\rangle = \delta\langle V^2\rangle/I^2$ depends quadratically on the source-drain bias V. This ensures that the measured $1/f$ is indeed from the device and that all spurious noise sources such as contact noise, amplifier noise, and other pick-up have been completely eliminated. Figure 8 shows the spectrum of $1/f$ noise and background noise of the WTe_2 device.

APPENDIX C: LORENTZIAN AND 1/F COMPONENTS OF NOISE

In a nonmagnetic conductor, there are two dominant sources of resistance fluctuations; charge carrier mobility fluctuations and charge carrier number density [60,61,75,76]. In high-number density metals, it is fluctuations in the carrier mobility determined, among other things, by phonon scattering [77,78]. On the other hand, in the case of low number density systems like WTe_2, the resistance noise is dominated by number density fluctuations [62]. In our system, the charge carrier number density fluctuations is the dominant source of noise. Figure 9 shows the contribution of $1/f$ and the Lorentzian component to the total noise. It is clear from the graph that the peak present in the total noise during the Lifshitz transition is not only from the 1/f component but also from the Lorentzian component. The origin of the temperature dependence of the noise is the $1/f$ component of the noise.

APPENDIX D: ESTIMATING THE QUANTUM LIFE TIME

The amplitude of the SdH oscillations related to the quantum life time τ_Q by the following expression [79–81]:

$$\delta R = 4R_0\chi(T)\exp(-\pi/\omega_c\tau_Q), \tag{D1}$$

where $\omega_c = eB/m^*$ is the cyclotron frequency and $\chi(T) = (2\pi^2 K_B T/\hbar\omega_c)/sinh(2\pi^2 K_B T/\hbar\omega_c)$ and R_0 is the resistance at zero magnetic field. τ_Q can be extracted from the slope of $ln((\delta R/4R_0)/\chi(T))$ versus $1/B$, Fig. 10 shows the Dingle plot of WTe_2/SiO_2 device at 2K. The pockets being very close to each other, it was not possible to calculate the τ_Q for each pocket individually. Instead, we calculated the average τ_Q using the Dingle plots. The τ_Q value estimated for the WTe_2/SiO_2 is 0.3 ps and for WTe_2/hBN is 0.25 ps.

APPENDIX E: ESTIMATING THE TRANSPORT LIFE TIME

To calculate the transport time, we measured the Hall resistance at 2K. We analyzed the Hall data (Fig. 11) using the two-band model:

$$\rho_{xy} = \frac{-B}{e}\frac{\left(n_e\mu_e^2 + n_h\mu_h^2\right) + B\mu_e^2\mu_h^2(n_e + n_h)}{(n_e\mu_e + n_h\mu_h)^2) + B^2\mu_e^2\mu_h^2(n_e + n^h)^2} \tag{E1}$$

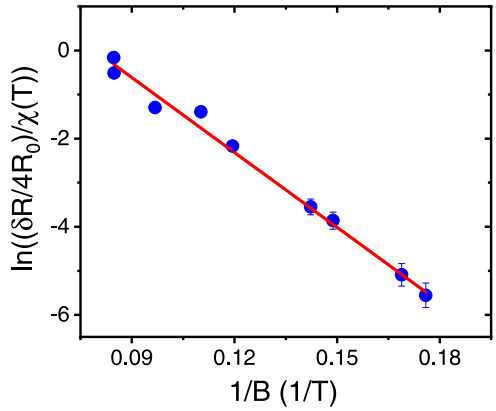

FIG. 10. Dingle plot for the amplitude of SdH oscillations measured at 2 K. The filled blue circles are the data points, the red line is the fit to extract the quantum lifetime τ_Q.

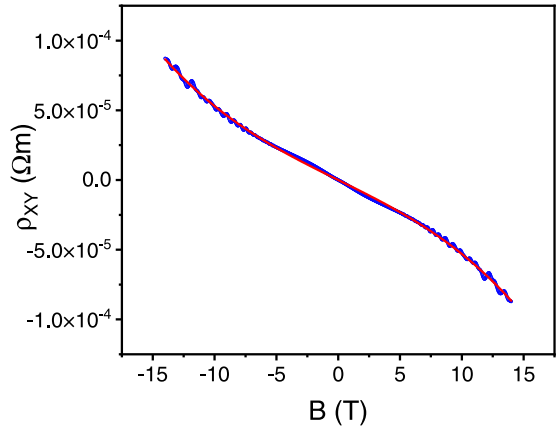

FIG. 11. Plot of Hall resistivity for WTe_2/SiO_2 device at 2K (blue open circle) and the fit to Eq. (E1) (red line).

with the constraint $\rho_{xy}(B=0) = (en_e\mu_e + en_h\mu_h)^{-1}$. Here n_e, μ_e, and n_h, μ_h are the carrier density and the mobility of electrons and holes, respectively. The μ_h, μ_e, n_h and n_e for WTe_2/SiO_2 device is 3,788 cm^2V/s, 21,318 cm^2V/s, 9.9×10^{17} cm^{-3} and 1×10^{18} cm^{-3}. For WTe_2/hBN device these values are 19 483 cm^2V/s, 24,504 cm^2V/s, 1×10^{18} cm^{-3} and 1×10^{18} cm^{-3}, respectively. The mobility of the holes is used to extract τ_{tr} using $\tau_{tr} = m^*\mu/e$. Here m^* is the effective mass extracted from Lifshitz-Kosevich equation. The τ_{tr} value estimated for the WTe_2/SiO_2 is 0.9 ps and for WTe_2/hBN is 7.5 ps.

[1] I. M. Lifshitz, Anomalies of electron characteristics in the high pressure region, Zh. Eksp. Teor. Fiz. **38**, 1130 (1960).

[2] Y. Wang, M. N. Gastiasoro, B. M. Andersen, M. Tomić, H. O. Jeschke, R. Valentí, I. Paul, and P. J. Hirschfeld, Effects of Lifshitz Transition on Charge Transport in Magnetic Phases of Fe-Based Superconductors, Phys. Rev. Lett. **114**, 097003 (2015).

[3] S. Beaulieu, S. Dong, N. Tancogne-Dejean, M. Dendzik, T. Pincelli, J. Maklar, R. P. Xian, M. A. Sentef, M. Wolf, A. Rubio, L. Rettig, and R. Ernstorfer, Ultrafast dynamical Lifshitz transition, Sci. Adv. **7**, eabd9275 (2021).

[4] K. Du, F.-T. Huang, J. Kim, S. J. Lim, K. Gamage, J. Yang, M. Mostovoy, J. Garlow, M.-G. Han, Y. Zhu, and S.-W. Cheong, Topological spin/structure couplings in layered chiral magnet $Cr_{1/3}TaS_2$: The discovery of spiral magnetic superstructure, Proc. Natl. Acad. Sci. USA **118**, e2023337118 (2021).

[5] H. Polshyn, Y. Zhang, M. A. Kumar, T. Soejima, P. Ledwith, K. Watanabe, T. Taniguchi, A. Vishwanath, M. P. Zaletel, and A. F. Young, Topological charge density waves at half-integer filling of a moiré superlattice, Nat. Phys. **18**, 42 (2022).

[6] M. M. Maśka, N. Sedlmayr, A. Kobiałka, and T. Domański, Unconventional topological transitions in a self-organized magnetic ladder, Phys. Rev. B **103**, 235419 (2021).

[7] W. Shi, B. J. Wieder, H. L. Meyerheim, Y. Sun, Y. Zhang, Y. Li, L. Shen, Y. Qi, L. Yang, J. Jena *et al.*, A charge-density-wave topological semimetal, Nat. Phys. **17**, 381 (2021).

[8] C.-Z. Li, A.-Q. Wang, C. Li, W.-Z. Zheng, A. Brinkman, D.-P. Yu, and Z.-M. Liao, Topological Transition of Superconductivity in Dirac Semimetal Nanowire Josephson Junctions, Phys. Rev. Lett. **126**, 027001 (2021).

[9] H. N. S. Krishnamoorthy, Z. Jacob, E. Narimanov, I. Kretzschmar, and V. M. Menon, Topological transitions in metamaterials, Science **336**, 205 (2012).

[10] S.-Y. Xu, Y. Xia, L. A. Wray, S. Jia, F. Meier, J. H. Dil, J. Osterwalder, B. Slomski, A. Bansil, H. Lin, R. J. Cava, and M. Z. Hasan, Topological phase transition and texture inversion in a tunable topological insulator, Science **332**, 560 (2011).

[11] L. Zhang, L. Zhang, and X.-J. Liu, Characterizing topological phases by quantum quenches: A general theory, Phys. Rev. A **100**, 063624 (2019).

[12] M. N. Ali, J. Xiong, S. Flynn, J. Tao, Q. D. Gibson, L. M. Schoop, T. Liang, N. Haldolaarachchige, M. Hirschberger, N. P. Ong, and R. J. Cava, Large, non-saturating magnetoresistance in WTe_2, Nature (London) **514**, 205 (2014).

[13] Y. Wang, L. Wang, X. Liu, H. Wu, P. Wang, D. Yan, B. Cheng, Y. Shi, K. Watanabe, T. Taniguchi, S.-J. Liang, and F. Miao, Direct evidence for charge compensation-induced large magnetoresistance in thin WTe_2, Nano Lett. **19**, 3969 (2019).

[14] D. Kang, Y. Zhou, W. Yi, C. Yang, J. Guo, Y. Shi, S. Zhang, Z. Wang, C. Zhang, S. Jiang *et al.*, Superconductivity emerging from a suppressed large magnetoresistant state in tungsten ditelluride, Nat. Commun. **6**, 7804 (2015).

[15] X.-C. Pan, X. Chen, H. Liu, Y. Feng, Z. Wei, Y. Zhou, Z. Chi, L. Pi, F. Yen, F. Song *et al.*, Pressure-driven dome-shaped superconductivity and electronic structural evolution in tungsten ditelluride, Nat. Commun. **6**, 7805 (2015).

[16] P. Lu, J.-S. Kim, J. Yang, H. Gao, J. Wu, D. Shao, B. Li, D. Zhou, J. Sun, D. Akinwande, D. Xing, and J.-F. Lin, Origin of superconductivity in the Weyl semimetal WTe_2 under pressure, Phys. Rev. B **94**, 224512 (2016).

[17] C. Huang, A. Narayan, E. Zhang, Y. Liu, X. Yan, J. Wang, C. Zhang, W. Wang, T. Zhou, C. Yi, S. Liu, J. Ling, H. Zhang,

R. Liu, R. Sankar, F. Chou, Y. Wang, Y. Shi, K. T. Law, S. Sanvito *et al.*, Inducing strong superconductivity in WTe_2 by a proximity effect, ACS Nano **12**, 7185 (2018).

[18] Q. Li, C. He, Y. Wang, E. Liu, M. Wang, Y. Wang, J. Zeng, Z. Ma, T. Cao, C. Yi, N. Wang, K. Watanabe, T. Taniguchi, L. Shao, Y. Shi, X. Chen, S.-J. Liang, Q.-H. Wang, and F. Miao, Proximity-induced superconductivity with subgap anomaly in type II Weyl semimetal WTe_2, Nano Lett. **18**, 7962 (2018).

[19] V. Fatemi, S. Wu, Y. Cao, L. Bretheau, Q. D. Gibson, K. Watanabe, T. Taniguchi, R. J. Cava, and P. Jarillo-Herrero, Electrically tunable low-density superconductivity in a monolayer topological insulator, Science **362**, 926 (2018).

[20] L. Zhu, Q.-Y. Li, Y.-Y. Lv, S. Li, X.-Y. Zhu, Z.-Y. Jia, Y. B. Chen, J. Wen, and S.-C. Li, Superconductivity in potassium-intercalated Td-WTe_2, Nano Lett. **18**, 6585 (2018).

[21] P. Sharma, F.-X. Xiang, D.-F. Shao, D. Zhang, E. Y. Tsymbal, A. R. Hamilton, and J. Seidel, A room-temperature ferroelectric semimetal, Sci. Adv. **5**, eaax5080 (2019).

[22] K. G. Rana, F. K. Dejene, N. Kumar, C. R. Rajamathi, K. Sklarek, C. Felser, and S. S. P. Parkin, Thermopower and unconventional Nernst effect in the predicted type-II Weyl semimetal WTe_2, Nano Lett. **18**, 6591 (2018).

[23] Z. Fei, T. Palomaki, S. Wu, W. Zhao, X. Cai, B. Sun, P. Nguyen, J. Finney, X. Xu, and D. H. Cobden, Edge conduction in monolayer WTe_2, Nat. Phys. **13**, 677 (2017).

[24] S. Wu, V. Fatemi, Q. D. Gibson, K. Watanabe, T. Taniguchi, R. J. Cava, and P. Jarillo-Herrero, Observation of the quantum spin Hall effect up to 100 kelvin in a monolayer crystal, Science **359**, 76 (2018).

[25] Y. Shi, J. Kahn, B. Niu, Z. Fei, B. Sun, X. Cai, B. A. Francisco, D. Wu, Z.-X. Shen, X. Xu, D. H. Cobden, and Y.-T. Cui, Imaging quantum spin Hall edges in monolayer WTe_2, Sci. Adv. **5**, eaat8799 (2019).

[26] P. K. Das, D. D. Sante, F. Cilento, C. Bigi, D. Kopic, D. Soranzio, A. Sterzi, J. A. Krieger, I. Vobornik, J. Fujii, T. Okuda, V. N. Strocov, M. B. H. Breese, F. Parmigiani, G. Rossi, S. Picozzi, R. Thomale, G. Sangiovanni, R. J. Cava, and G. Panaccione, Electronic properties of candidate type-II Weyl semimetal WTe_2. A review perspective, Electron. Struct. **1**, 014003 (2019).

[27] X.-C. Pan, X. Wang, F. Song, and B. Wang, The study on quantum material WTe_2, Adv. Phys.: X **3**, 1468279 (2018).

[28] A. A. Soluyanov, D. Gresch, Z. Wang, Q. Wu, M. Troyer, X. Dai, and B. A. Bernevig, Type-II Weyl semimetals, Nature (London) **527**, 495 (2015).

[29] H. Zheng and M. Z. Hasan, Quasiparticle interference on type-I and type-II Weyl semimetal surfaces: A review, Adv. Phys.: X **3**, 1466661 (2018).

[30] K. Deng, G. Wan, P. Deng, K. Zhang, S. Ding, E. Wang, M. Yan, H. Huang, H. Zhang, Z. Xu *et al.*, Experimental observation of topological Fermi arcs in type-II Weyl semimetal $MoTe_2$, Nat. Phys. **12**, 1105 (2016).

[31] C. Wang, Y. Zhang, J. Huang, S. Nie, G. Liu, A. Liang, Y. Zhang, B. Shen, J. Liu, C. Hu, Y. Ding, D. Liu, Y. Hu, S. He, L. Zhao, L. Yu, J. Hu, J. Wei, Z. Mao, Y. Shi *et al.*, Observation of Fermi arc and its connection with bulk states in the candidate type-II Weyl semimetal WTe_2, Phys. Rev. B **94**, 241119(R) (2016).

[32] P. Li, W. Wu, Y. Wen, C. Zhang, J. Zhang, S. Zhang, Z. Yu, S. A. Yang, A. Manchon, and X.-x. Zhang, Spin-momentum locking and spin-orbit torques in magnetic nano-heterojunctions composed of Weyl semimetal WTe_2, Nat. Commun. **9**, 3990 (2018).

[33] K. Takiguchi, Y. K. Wakabayashi, H. Irie, Y. Krockenberger, T. Otsuka, H. Sawada, S. A. Nikolaev, H. Das, M. Tanaka, Y. Taniyasu *et al.*, Quantum transport evidence of Weyl fermions in an epitaxial ferromagnetic oxide, Nat. Commun. **11**, 4969 (2020).

[34] E. V. Gorbar, V. A. Miransky, I. A. Shovkovy, and P. O. Sukhachov, Origin of dissipative Fermi arc transport in Weyl semimetals, Phys. Rev. B **93**, 235127 (2016).

[35] P. Rüßmann, A. P. Weber, F. Glott, N. Xu, M. Fanciulli, S. Muff, A. Magrez, P. Bugnon, H. Berger, M. Bode, J. H. Dil, S. Blügel, P. Mavropoulos, and P. Sessi, Universal scattering response across the type-II Weyl semimetal phase diagram, Phys. Rev. B **97**, 075106 (2018).

[36] S. Sykora, J. Schoop, L. Graf, G. Shipunov, I. V. Morozov, S. Aswartham, B. Büchner, C. Hess, R. Giraud, and J. Dufouleur, Disorder-induced coupling of Weyl nodes in WTe_2, Phys. Rev. Res. **2**, 033041 (2020).

[37] Y. Wu, N. H. Jo, M. Ochi, L. Huang, D. Mou, S. L. Bud'ko, P. C. Canfield, N. Trivedi, R. Arita, and A. Kaminski, Temperature-induced Lifshitz transition in WTe_2, Phys. Rev. Lett. **115**, 166602 (2015).

[38] Q. Zhang, Z. Liu, Y. Sun, H. Yang, J. Jiang, S.-K. Mo, Z. Hussain, X. Qian, L. Fu, S. Yao, M. Lu, C. Felser, B. Yan, Y. Chen, and L. Yang, Lifshitz transitions induced by temperature and surface doping in type-II Weyl semimetal candidate Td-WTe_2, Phys. Status Solidi RRL **11**, 1700209 (2017).

[39] A. E. M. Smink, J. C. de Boer, M. P. Stehno, A. Brinkman, W. G. van der Wiel, and H. Hilgenkamp, Gate-Tunable Band Structure of the $LaAlO_3-SrTiO_3$ Interface, Phys. Rev. Lett. **118**, 106401 (2017).

[40] X. Wang, D. Pan, Q. Zeng, X. Chen, H. Wang, D. Zhao, Z. Xu, Q. Yang, J. Deng, T. Zhai, G. Wu, E. Liu, and J. Zhao, Robust anomalous Hall effect and temperature-driven Lifshitz transition in Weyl semimetal Mn_3Ge, Nanoscale **13**, 2601 (2021).

[41] S. Galeski, T. Ehmcke, R. Wawrzyńczak, P. M. Lozano, K. Cho, A. Sharma, S. Das, F. Küster, P. Sessi, M. Brando *et al.*, Origin of the quasiquantized Hall effect in $ZrTe_5$, Nat. Commun. **12**, 3197 (2021).

[42] K. S. Novoselov, A. K. Geim, S. V. Morozov, D. Jiang, Y. Zhang, S. V. Dubonos, I. V. Grigorieva, and A. A. Firsov, Electric field effect in atomically thin carbon films, Science **306**, 666 (2004).

[43] M. A. Meitl, Z.-T. Zhu, V. Kumar, K. J. Lee, X. Feng, Y. Y. Huang, I. Adesida, R. G. Nuzzo, and J. A. Rogers, Transfer printing by kinetic control of adhesion to an elastomeric stamp, Nat. Mater. **5**, 33 (2006).

[44] X. Liang, Z. Fu, and S. Y. Chou, Graphene transistors fabricated via transfer-printing in device active-areas on large wafer, Nano Lett. **7**, 3840 (2007).

[45] https://www.2dsemiconductors.com/

[46] S. S., H. K. Kundu, P. Vishnubhotla, and A. Bid, Hidden electronic phase in strained few-layer 1T-TaS_2, Phys. Rev. Mater. **5**, 124003 (2021).

[47] C. R. Dean, A. F. Young, I. Meric, C. Lee, L. Wang, S. Sorgenfrei, K. Watanabe, T. Taniguchi, P. Kim, K. L. Shepard *et al.*, Boron nitride substrates for high-quality graphene electronics, Nat. Nanotechnol. **5**, 722 (2010).

[48] Y. L. Wang, L. R. Thoutam, Z. L. Xiao, J. Hu, S. Das, Z. Q. Mao, J. Wei, R. Divan, A. Luican-Mayer, G. W. Crabtree, and W. K. Kwok, Origin of the turn-on temperature behavior in WTe_2, Phys. Rev. B **92**, 180402(R) (2015).

[49] K. Behnia and H. Aubin, Nernst effect in metals and superconductors: A review of concepts and experiments, Rep. Prog. Phys. **79**, 046502 (2016).

[50] E. H. Hwang, E. Rossi, and S. Das Sarma, Theory of thermopower in two-dimensional graphene, Phys. Rev. B **80**, 235415 (2009).

[51] Y. K. Kuo, K. M. Sivakumar, H. C. Chen, J. H. Su, and C. S. Lue, Anomalous thermal properties of the Heusler alloy $Ni_{2+x}Mn_{1-x}Ga$ near the martensitic transition, Phys. Rev. B **72**, 054116 (2005).

[52] F.-X. Xiang, M. Veldhorst, S.-X. Dou, and X.-L. Wang, Multiple Fermi pockets revealed by Shubnikov–de Haas oscillations in WTe_2, Europhys. Lett. **112**, 37009 (2015).

[53] P. Li, Y. Wen, X. He, Q. Zhang, C. Xia, Z.-M. Yu, S. A. Yang, Z. Zhu, H. N. Alshareef, and X.-X. Zhang, Evidence for topological type-II Weyl semimetal WTe_2, Nat. Commun. **8**, 2150 (2017).

[54] C. Guo, A. Alexandradinata, C. Putzke, A. Estry, T. Tu, N. Kumar, F.-R. Fan, S. Zhang, Q. Wu, O. V. Yazyev *et al.*, Temperature dependence of quantum oscillations from non-parabolic dispersions, Nat. Commun. **12**, 6213 (2021).

[55] D. Shoenberg, *Magnetic Oscillations in Metals*, Cambridge Monographs on Physics (Cambridge University Press, Cambridge, 1984).

[56] H. K. Kundu, S. Ray, K. Dolui, V. Bagwe, P. R. Choudhury, S. B. Krupanidhi, T. Das, P. Raychaudhuri, and A. Bid, Quantum Phase Transition in Few-Layer Probed Through Quantized Cconductance Fluctuations, Phys. Rev. Lett. **119**, 226802 (2017).

[57] G. N. Daptary, C. Sow, P. S. Anil Kumar, and A. Bid, Probing a spin-glass state in $SrRuO_3$ thin films through higher-order statistics of resistance fluctuations, Phys. Rev. B **90**, 115153 (2014).

[58] M. B. Weissman, $\frac{1}{f}$ noise and other slow, nonexponential kinetics in condensed matter, Rev. Mod. Phys. **60**, 537 (1988).

[59] P. Dutta, P. Dimon, and P. M. Horn, Energy Scales for Noise Processes in Metals, Phys. Rev. Lett. **43**, 646 (1979).

[60] F. Hooge, 1/f noise sources, IEEE Trans. Electron Devices **41**, 1926 (1994).

[61] F. N. Hooge, T. G. M. Kleinpenning, and L. K. J. Vandamme, Experimental studies on 1/f noise, Rep. Prog. Phys. **44**, 479 (1981).

[62] G. N. Daptary, P. Kumar, A. Dogra, and A. Bid, Effect of multiband transport on charge carrier density fluctuations at the $LaAlO_3/SrTiO_3$ interface, Phys. Rev. B **98**, 035433 (2018).

[63] Z. Huang, D. P. Arovas, and A. V. Balatsky, Impurity scattering in Weyl semimetals and their stability classification, New J. Phys. **15**, 123019 (2013).

[64] D. Culcer, E. H. Hwang, T. D. Stanescu, and S. Das Sarma, Two-dimensional surface charge transport in topological insulators, Phys. Rev. B **82**, 155457 (2010).

[65] C.-L. Zhang, Z. Yuan, Q.-D. Jiang, B. Tong, C. Zhang, X. C. Xie, and S. Jia, Electron scattering in tantalum monoarsenide, Phys. Rev. B **95**, 085202 (2017).

[66] S. Sarkar, K. R. Amin, R. Modak, A. Singh, S. Mukerjee, and A. Bid, Role of different scattering mechanisms on the temperature dependence of transport in graphene, Sci. Rep. **5**, 16772 (2015).

[67] J.-Z. Ma, S. M. Nie, C. J. Yi, J. Jandke, T. Shang, M. Y. Yao, M. Naamneh, L. Q. Yan, Y. Sun, A. Chikina, V. N. Strocov, M. Medarde, M. Song, Y.-M. Xiong, G. Xu, W. Wulfhekel, J. Mesot, M. Reticcioli, C. Franchini, C. Mudry *et al.*, Spin fluctuation induced Weyl semimetal state in the paramagnetic phase of $EuCd_2As_2$, Sci. Adv. **5**, eaaw4718 (2019).

[68] T. Schumann, M. Goyal, D. A. Kealhofer, and S. Stemmer, Negative magnetoresistance due to conductivity fluctuations in films of the topological semimetal Cd_3As_2, Phys. Rev. B **95**, 241113(R) (2017).

[69] J. H. Scofield, ac method for measuring low frequency resistance fluctuation spectra, Rev. Sci. Instrum. **58**, 985 (1987).

[70] J. S. Moon, A. F. Mohamedulla, and N. O. Birge, Digital measurement of resistance fluctuations, Rev. Sci. Instrum. **63**, 4327 (1992).

[71] F. Reif, *Fundamentals of Statistical and Thermal Physics* (Waveland Press, Long Grove, IL, 2009).

[72] R. Koushik, S. Kumar, K. R. Amin, M. Mondal, J. Jesudasan, A. Bid, P. Raychaudhuri, and A. Ghosh, Correlated Conductance Fluctuations Close to the Berezinskii-Kosterlitz-Thouless Transition in Ultrathin NbN Films, Phys. Rev. Lett. **111**, 197001 (2013).

[73] G. N. Daptary, S. Kumar, P. Kumar, A. Dogra, N. Mohanta, A. Taraphder, and A. Bid, Correlated non-Gaussian phase fluctuations in $LaAlO_3/SrTiO_3$ heterointerfaces, Phys. Rev. B **94**, 085104 (2016).

[74] S. Sarkar, A. Bid, K. L. Ganapathi, and S. Mohan, Probing defect states in few-layer MoS_2 by conductance fluctuation spectroscopy, Phys. Rev. B **99**, 245419 (2019).

[75] R. Jayaraman and C. Sodini, A 1/f noise technique to extract the oxide trap density near the conduction band edge of silicon, IEEE Trans. Electron Devices **36**, 1773 (1989).

[76] A. L. McWhorter, 1/f Noise and Related Surface Effects in Germanium, MIT Lincoln Laboratory Report No. 80, May, 1955.

[77] J. P. Harrang, R. J. Higgins, R. K. Goodall, P. R. Jay, M. Laviron, and P. Delescluse, Quantum and classical mobility determination of the dominant scattering mechanism in the two-dimensional electron gas of an AlGaAs/GaAs heterojunction, Phys. Rev. B **32**, 8126 (1985).

[78] E. H. Hwang and S. Das Sarma, Acoustic phonon scattering limited carrier mobility in two-dimensional extrinsic graphene, Phys. Rev. B **77**, 115449 (2008).

[79] P. T. Coleridge, R. Stoner, and R. Fletcher, Low-field transport coefficients in $GaAs/Ga_{1-x}Al_xAs$ heterostructures, Phys. Rev. B **39**, 1120 (1989).

[80] P. T. Coleridge, Small-angle scattering in two-dimensional electron gases, Phys. Rev. B **44**, 3793 (1991).

[81] Q. Qian, J. Nakamura, S. Fallahi, G. C. Gardner, J. D. Watson, S. Lüscher, J. A. Folk, G. A. Csáthy, and M. J. Manfra, Quantum lifetime in ultrahigh quality GaAs quantum wells: Relationship to $\Delta_{5/2}$ and impact of density fluctuations, Phys. Rev. B **96**, 035309 (2017).